IEEE Access
Multidisciplinary | Rapid Review | Open Access Journal

Received July 14, 2019, accepted July 23, 2019, date of publication July 30, 2019, date of current version August 23, 2019.

Digital Object Identifier 10.1109/ACCESS.2019.2932090

Spherical Equivalent Dipole Array Theory and Its Applications to Complex Electromagnetic System

JING NIE, SHUNCHUAN YANG, (Member, IEEE), AND DONGLIN SU, (Member, IEEE)
School of Electronic and Information Engineering, Institute of Electromagnetic Compatibility Technology, Beihang University, Beijing 100191, China

Corresponding author: Donglin Su (sdl@buaa.edu.cn)

This work was supported by the National Natural Science Foundation of China under Grant 61427803.

ABSTRACT The equivalent dipole array is an effective method for emission source modeling to solve practical electromagnetic engineering problems. In this paper, a spherical equivalent dipole array method (SEDAM) is proposed to model practical and complex electronic systems. Unlike the planar equivalent dipole array method (PEDAM), SEDAM is derived in the spherical coordinate system and is more suitable for large electromagnetic equipments. In addition, SEDAM can achieve accurate emission prediction around electronic systems of arbitrary structures, where PEDAM is not easy to be used. We first derived the analytical relationship between magnetic fields and magnetic dipole moments in the spherical coordinate system. To model the complex systems, several equivalent dipoles are properly placed on a spherical surface which encloses the equipment under test (EUT). By superposition of the fields generated by all the equivalent dipoles, the equivalent relational matrix is constructed and the weights for each dipole are solved. Then, the weighted dipole array can be used to predict the emission fields at desired locations. The proposed method is first verified through a numerical simulation. The results show that the proposed SEDAM outperforms the PEDAM in terms of accuracy. It is further validated through a measurement. The measurement results show that SEDAM can model the practical and complex electronic systems and predict their electromagnetic emission with acceptable accuracy.

INDEX TERMS Electromagnetic compatibility, equivalence, interference source location, radiation source, spherical dipole array.

I. INTRODUCTION

The emission characteristics of complex electronic systems have been becoming increasingly important to identify the electromagnetic compatibility (EMC) issues [1]. Recently, the ''basic emission waveform theory'' is proposed with emphasis on the physical characteristics of systems with four basic waveforms, which realize emission characteristic extraction and recognition of various emission sources according to inherent physical properties [2]. When the structural parameters of complex systems can not be obtained accurately or even unavailable, the EUT is just like a ''black box'' and the full-wave simulation can not be performed. Then, it is desirable to use the equivalent methods to model such systems. Two main categories of methods draw attention and we briefly summarize the researches.

A. SOURCE PREDICTION

In terms of source prediction, plane wave and spherical wave expansion methods are used to predict emission sources of complex systems. Many efforts have been done in the last decades to improve their accuracy [3]–[6]. According to the Huygens' principle, the spherical near-field measurement is suitable to reflect the electromagnetic emission characteristics of systems. In [7], a spherical near-field (SNF) far-field transformation procedure including pointwise probe correction was proposed. In [8], standard wideband antennas as probes are used to analyze modern multi-service antenna systems. Another method for hemispherical near-field antenna measurements is proposed and shows good performance [9]. It is worth emphasizing that the high accuracy of the testing probe needs to be ensured using the method above, which is hard to realize.

B. SOURCE EQUIVALENCE

In terms of source equivalence, as electronic systems become more complex, full-wave methods can not meet the needs of EMC modeling due to extremely large computational resource consumptions. Then, the equivalent methods are proposed in the last decades. Based on the measurement of original systems, the equivalent current elements and

The associate editor coordinating the review of this manuscript and approving it for publication was Amedeo Andreotti.

magnetic elements were used to replace original systems, and then through some numerical methods, the emission of equivalent sources were calculated to realize the prediction of emission characteristics of original complex systems in [10], [11].

In fact, the electric and magnetic dipoles are the most idealized electromagnetic radiation units. The PEDAM was proposed and has been widely used in the near-field scanning equivalent modeling, which is quite suitable to model integrated circuits and printed circuit boards (PCBs) [12]–[19]. For example, the equivalent dipole moments models and a decomposition method based on the reciprocity theory were proposed to evaluate the coupling between the noise sources and the victim antennas [20]. A machine learning based source reconstruction method is developed to extract the equivalent dipole moments accurately and reliably in [21]. A method is proposed to predict the maximum far-field emission based on phaseless near-field scanning with dominant magnetic dipoles from PCBs [22]. In [23], an efficient equivalent dipole moments method is proposed to predict the emission from PCBs installed in a shielding cavity. In the methods above, all the equivalent dipoles are placed on planar surfaces.

In practice, the PEDAMs are suitable for modeling in the reactive near-field region with high complexity of data acquisition and large scale of sampling data. Furthermore, they are limited by the size of the scanning plane and can only predict the planar fields distribution outside the scanning plane. To overcome this limitation of the PEDAMs, in this paper, we proposed a SEDAM to model complex electronic systems, which is more suitable for the large-scale system compared with the PEDAMs. The proposed method can be used to model in radiation near-field region, which requires less sampling data. In addition, it has advantages in predicting and analyzing the omnidirectional radiation emission of systems. It's particularly useful for interference source location where near-field noise coupling needs to be accurately analyzed.

Three folds of contributions in this paper are summarized as follows.

1) The SEDAM is proposed in spherical coordinate system, which takes the three-dimensional space direction electromagnetic emission of electronic equipment into account, and the derivation including all the equivalent points and the magnetic fields in the three directions of r, θ and ϕ.
2) The SEDAM is verified through a full-wave simulation for Multiple-Input Multiple-Output (MIMO) Ring antenna and an experiment, respectively. The electromagnetic emission prediction results from various fields including the near-field magnetic fields, far-field magnetic/electric fields and far-field direction patterns can be obtained with acceptable accuracy.
3) The proposed method is compared with the PEDAM. By establishing equivalent models at the same equivalent distance, the two models predictive effectiveness of the far-field are analyzed. The proposed method is more suitable for large electromagnetic equipment, where the PEDAM is not easy to be used.

However, we also observe some limitations of the proposed method. When the sampling points make values of trigonometric function equal to zero, which means there are several zero terms in the relational matrix T, the condition number is too large for matrix inversion. The error can be quite large. Therefore, sampling points should be set as far away from the spherical poles and the equator as possible.

The paper is organized as follows. In Section II, the theory of SEDAM is introduced. In Section III, numerical examples are carried out to validate the accuracy of the proposed method. In Section IV, the method in this paper is compared with the PEDAM in simulation. In Section V, the SEDAM and PEDAM are further validated by a practical experiment. At last, we draw some conclusions in Section VI.

II. THE THEORY OF BASIC THEORY OF SPHERICAL EQUIVALENT DIPOLE ARRAY

The equivalent dipole array theory was first proposed by P. Wilson in 1995 [24]. According to the equivalence of the fields generated by the electric or magnetic dipoles and the original systems, an array of weighted dipoles can be deduced to represent the original emission characteristics.

The fields in spherical coordinates due to a single vertical electric dipole P_z and a magnetic dipole M_z in free space can be expressed as bellow [24].

A vertical electric dipole:

$$E_r = k_0^2\sqrt{\frac{\mu_0}{\varepsilon_0}}\frac{P_z}{2\pi}\left[\frac{1}{(k_0r)^2} - \frac{j}{(k_0r)^3}\right]\cos\theta e^{-jk_0r}, \tag{1}$$

$$E_\theta = jk_0^2\sqrt{\frac{\mu_0}{\varepsilon_0}}\frac{P_z}{4\pi}\left[\frac{1}{k_0r} - \frac{j}{(k_0r)^2} - \frac{1}{(k_0r)^3}\right]\sin\theta e^{-jk_0r}, \tag{2}$$

$$H_\phi = jk_0^2\frac{P_z}{4\pi}\left[\frac{1}{k_0r} - \frac{j}{(k_0r)^2}\right]\sin\theta e^{-jk_0r}, \tag{3}$$

$$E_\phi = H_r = H_\theta = 0. \tag{4}$$

A vertical magnetic dipole:

$$H_r = k_0^3\frac{M_z}{2\pi}\left[\frac{j}{(k_0r)^2} + \frac{1}{(k_0r)^3}\right]\cos\theta e^{-jk_0r}, \tag{5}$$

$$H_\theta = -k_0^3\frac{M_z}{4\pi}\left[\frac{1}{k_0r} - \frac{j}{(k_0r)^2} - \frac{1}{(k_0rnn)^3}\right]\sin\theta e^{-jk_0r}, \tag{6}$$

$$E_\phi = k_0^3\sqrt{\frac{\mu_0}{\varepsilon_0}}\frac{M_z}{4\pi}\left[\frac{1}{k_0r} - \frac{j}{(k_0r)^2}\right]\sin\theta e^{-jk_0r}, \tag{7}$$

$$E_r = E_\theta = H_\phi = 0. \tag{8}$$

Other components can be easily obtained through the permutation of the coordinate variables, x, y and z based on Equ. (1)∼(8). Unlike the conventional PEDAM, in which the dipoles are placed in a single or several planar surfaces, and fields are derived from the Cartesian system, we proposed to place the dipole array in a spherical surface. Therefore, it would be more convenient to express the fields in the

spherical system. In the following, we present the detailed derivation.

It is found that the wave impedance of the electric and magnetic dipoles show totally different behaviors when the distance between the source and observation point, r, approaches 0. For the electric dipole, its wave impedance goes infinity, however, for the magnetic dipole, its wave impedance monotonically decreases to 0 [22]. Therefore, to avoid large numerical errors for the near-field measured data in the proposed method, magnetic dipoles (magnetic dipole moments) are selected as basic emission units and an array of magnetic dipoles distributed on a spherical surface are used to model complex electronic systems in this paper.

The magnetic dipole moments in the spherical system can be expressed in terms of their Cartesian components as

$$M_r = M_x \sin\theta_n \cos\phi_n + M_y \sin\theta_n \sin\phi_n + M_z \cos\theta_n, \tag{9}$$

$$M_\theta = M_x \cos\theta_n \cos\phi_n + M_y \cos\theta_n \sin\phi_n - M_z \sin\theta_n, \tag{10}$$

$$M_\phi = -M_x \sin\phi_n + M_y \cos\phi_n. \tag{11}$$

where (r_n, θ_n, ϕ_n) is the coordinate of equivalent point in the spherical coordinate system. Therefore, the magnetic fields due to a single magnetic dipole can be expressed as

$$H_r^m = K_h k_0 (T_{H_r M_r} M_r + T_{H_r M_\theta} M_\theta + T_{H_r M_\phi} M n n_\phi), \tag{12}$$

$$H_\theta^m = K_h k n n_0 (T_{H_\theta M n_r} M_r + T_{H_\theta M_\theta} M_\theta + T_{H_\theta M_\phi} M_\phi), \tag{13}$$

$$H_\phi^m = K_h k_0 (T_{H_\phi M_r} M_r + T_{H_\phi M_\theta} M_\theta + T_{H_\phi M_\phi} M_\phi). \tag{14}$$

where H_r^m, H_θ^m, H_ϕ^m are three components of the magnetic fields in spherical system, M_r, M_θ, M_ϕ are three components of the magnetic dipole moments, $k_0 = \frac{2\pi}{\lambda}$ is the wavenumber in free space, $K_h = \frac{k_0}{4\pi}$ is a constant associated with k_0. $T_{H_r M_r}, T_{H_r M_\theta}, T_{H_r M_\phi}, T_{H_\theta M_r}, T_{H_\theta M_\theta}, T_{H_\theta M_\phi}, T_{H_\phi M_r}, T_{H_\phi M_\theta}, T_{H_\phi M_\phi}$ are the conversion coefficients between $H_r^m, H_\theta^m, H_\phi^m$ and the three components of the dipole moments M_r, M_θ, M_ϕ in (12)∼(14), respectively, and are used to construct the relational matrix T.

Assuming that we have N observation points and N equivalent points, where the coordinates of the observation points are (r_m, θ_m, ϕ_m), $m = 1, \ldots, N$, the coordinates of the equivalent points are (r_n, θ_n, ϕ_n), $n = 1, \ldots, N$. By rewriting all the fields at the observation points into matrix form, we can obtain

$$K_h \cdot k_0 \cdot [T]_{3N\times 3N} \cdot [M]_{3N\times 1} = [H]_{3N\times 1} \tag{15}$$

where T is

$$T = \begin{bmatrix} [T_{H_r M_r}]_{N\times N} & [T_{H_r M_\theta}]_{N\times N} & [T_{H_r M_\phi}]_{N\times N} \\ [T_{H_\theta M_r}]_{N\times N} & [T_{H_\theta M n n_\theta}]_{N\times N} & [T_{H_\theta M n_\phi}]_{N\times N} \\ [T_{H_\phi M n n_r}]_{N\times N} & [T_{H_\phi M_\theta}]_{N\times N} & [T_{H_\phi M_\phi}]_{N\times N} \end{bmatrix} \tag{16}$$

where M and H are

$$M = \begin{bmatrix} [M_r]_{N\times 1} \\ [M_\theta]_{N\times 1} \\ [M_\phi]_{N\times 1} \end{bmatrix}, \quad H = \begin{bmatrix} [H_r]_{N\times 1} \\ [H_\theta]_{N\times 1} \\ [H_\phi]_{N\times 1} \end{bmatrix}. \tag{17}$$

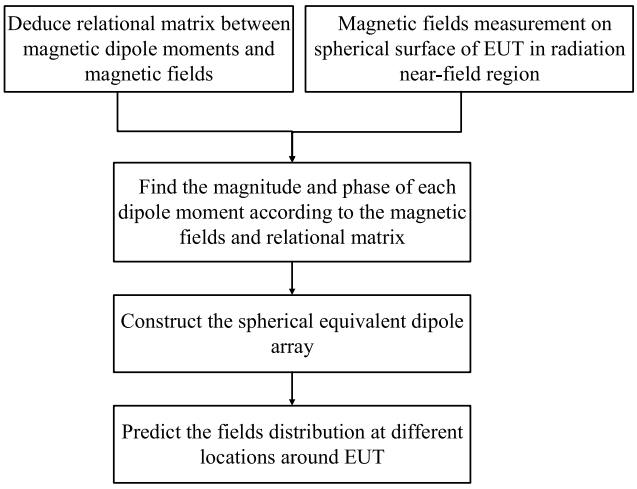

FIGURE 1. The flow chart of the SEDAM.

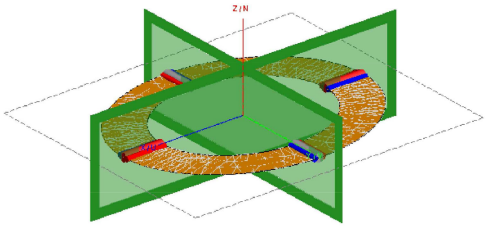

FIGURE 2. The MIMO ring antenna model.

The detailed expressions of each element in T can be found in the appendix section. Once we have the measured data at the observation points, the weights for each dipole can be solved through Equ. (15). Then, we can use those weighted dipoles distributed on a spherical surface to predict the electromagnetic emission of EUT. In the next two sections, we present several examples to demonstrate the effectiveness and accuracy of the proposed method.

III. THE NUMERICAL VERIFICATION WITH A MIMO RING ANTENNA

In this paper, the software FEldberechnung für Körper mit beliebiger Oberfläche (FEKO) is used to perform equivalent modeling for a MIMO ring antenna as shown in Fig. 2. The radius of the ring antenna is 0.0325m, and the frequency is $f = 2.4GHz$. In the simulation, the ranges of θ and ϕ are $1° \sim 179°$, $0° \sim 330°$, respectively, and the overall count of $7 \times 12 = 84$ observation points are selected at an interval of 30° both in θ and ϕ.

The wavelength is $\lambda = 0.125m$ and the diameter is $D = 0.065m$. According to $0.62\sqrt{\frac{D^3}{\lambda}} = 0.0291m$, $\frac{2D^2}{\lambda} = 0.0676m$, it's obvious that in the reactive near-field region, $r < 0.62\sqrt{\frac{D^3}{\lambda}} = 0.0291m$ is less than $\frac{D}{2} = 0.0325m$. Therefore, between the distance of 0.0325m and 0.0676m, we select the observed spherical surface with a radius $r_m = 0.062m$. We find that the optimal equivalent surface is

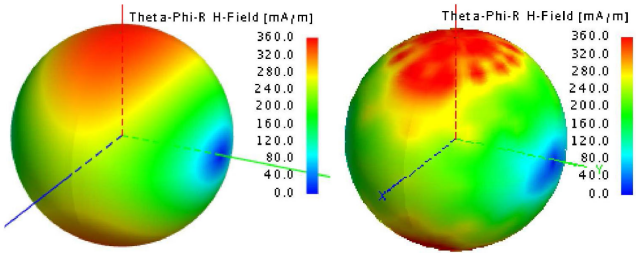

(a) Original magnetic field (b) Equivalent magnetic field

FIGURE 3. **Comparison of magnetic field distribution at 0.062 m.**

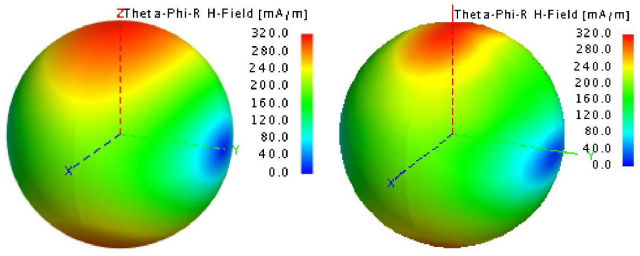

(a) Original magnetic field. (b) Equivalent magnetic field.

FIGURE 4. **Comparison of magnetic field distribution at 0.072 m.**

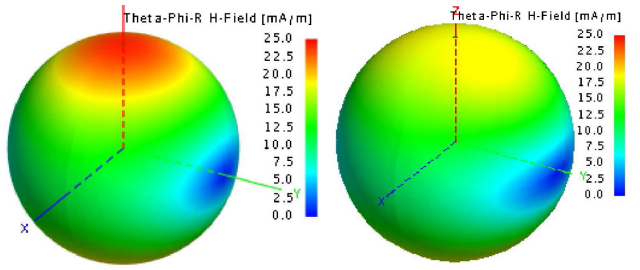

(a) Original magnetic field. (b) Equivalent magnetic field.

FIGURE 5. **Comparison of magnetic field distribution at 1 m.**

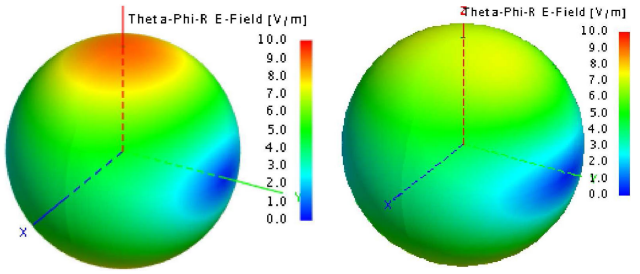

(a) Original electric field. (b) Equivalent electric field.

FIGURE 6. **Comparison of electric field distribution at 1 m.**

$r_n = 0.05m$. Through the analysis of the proposed method, the results are shown in Fig. 3∼ Fig. 6.

Fig. 3 shows the magnetic fields obtained from the full-wave simulation of the MIMO ring antenna and the proposed method on a spherical surface with the radius 0.062m in the radiation near-field region. The pattern of magnetic fields obtained from the two methods are approximately the same. By analyzing the results of all the observation points, it is shown that the component with the largest error is H_r, and the observation points with large errors are almost around the poles of the observation surface.

Fig. 4 shows the magnetic fields obtained from the two methods on a spherical surface with the radius 0.072m. The patterns of fields are almost the same. However, the values at the top show some differences. The components with larger errors are H_r and H_ϕ, the observation points with large errors are near the equator of the spherical surface.

Fig. 5-6 show the magnetic and electric fields at a spherical surface with the radius 1 m. It is found that the maximum magnetic and electric fields obtained from the proposed method are smaller than the full-wave simulation results, especially, near the top of the sphere. The component with the largest error is H_r, the observation points with large errors are both around the poles of the sphere and near the equator under the situation of 1 m.

When θ_m around 0°, 90°, 180°, their trigonometric function approaches 0, which causes the largest deviations. It's easy to find that H_r includes multiple terms of $sin\theta_m$ and $cos\theta_m$. In addition, as r increases, which is the denominator, elements for H_r in T including r becomes smaller. Therefore, H_r basically shows the largest error in those observation points. In our implementation, we skipped those angles to avoid large errors.

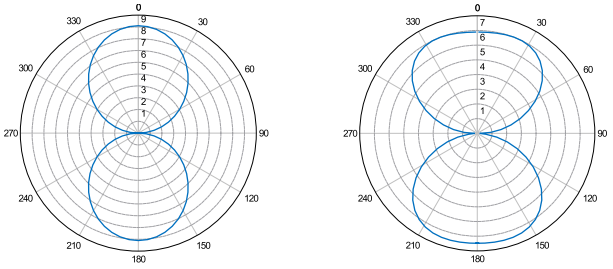

(a) Original model. (b) Equivalent model.

FIGURE 7. **Comparison of far-field direction pattern at $\phi = 90°$, total *E* magnitude (*V*).**

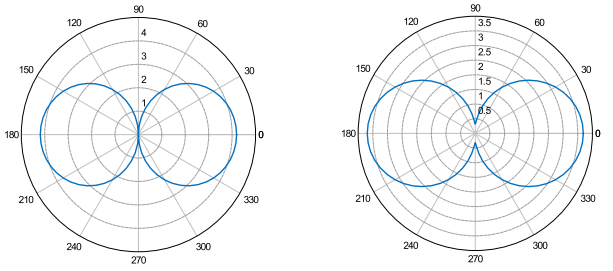

(a) Original model. (b) Equivalent model.

FIGURE 8. **Comparison of far-field direction pattern at $\theta = 90°$, total *E* magnitude (*V*).**

The far-field direction patterns of the original model and the equivalent model are shown in Fig. 7, 8 with $\phi = 90°$

and $\theta = 90°$, respectively. It is easy to find that no matter whether $\phi = 90°$ and $\theta = 90°$, the distribution of the far-field direction is roughly the same, but the amplitude of the equivalent model is relatively small.

We investigate the error of the proposed method. The error is defined as follows.

$$Error(H_k) = \sqrt{\frac{\Sigma_{i=1}^{N}(M_s(H_k(i)) - M_e(H_k(i)))^2}{\Sigma_{i=1}^{N}(M_s(H_k(i)))^2}}, \quad (18)$$

$$Error(E_k) = \sqrt{\frac{\Sigma_{i=1}^{N}(M_s(E_k(i)) - M_e(E_k(i)))^2}{\Sigma_{i=1}^{N}(M_s(E_k(i)))^2}}. \quad (19)$$

where H_k and E_k are magnetic and electric fields component, respectively, M_s is the magnetic fields truth value of the original source, and M_e is the magnetic fields truth value of the equivalent source. N is the total number of sampling points, $i = 1, 2, \ldots, N$. $k = r, \theta, \phi, x, y, z$. The error is indicated by the mean squared error (MSE) between the original near-field intensities $M_s(H_k)$ (or $M_s(E_k)$) and the equivalent near-field intensities $M_e(H_k)$ (or $M_e(E_k)$). The results from Table 1∼ Table 4 are all according to Equ. (18) and (19).

TABLE 1. The applicability and limitations of the two methods.

Method	Planar structure system	Non-planar structure system	Full space accurate prediction	Demanding of sampling points is weak
SEDAM	√	√	√	×
PEDAM	√	×	×	√

TABLE 2. The error of 84 equivalent points.

Distance	0.062m magnetic	0.072m magnetic	1 m magnetic	1 m electric
$Error(r)$	0.0026	0.2050	0.1710	0.2790
$Error(\theta)$	0.0013	0.0585	0.1703	0.1594
$Error(\phi)$	0.0013	0.0963	0.1596	0.1701

TABLE 3. The error of 289 equivalent points.

Distance	0.062m magnetic	0.072m magnetic	1 m magnetic	1 m electric
$Error(x)$	0.0012	0.0376	0.1780	1.2800
$Error(y)$	0.0099	0.7123	0.5482	0.1778
$Error(z)$	0.0024	0.1484	0.1590	0.1284

TABLE 4. The error of 289 equivalent points at 0:001 M.

Distance	0.01m magnetic	0.02m magnetic	1 m magnetic
$Error$	0.0002	0.0081	0.0272

The equivalent accuracy of the measured surface 0.062m magnetic fields, the observation surface 0.072m magnetic fields in near-field and observation surface 1 m electric/ magnetic fields distribution in far-field are, respectively, shown in Table 2. From the Table 2, both in the near-field and far-field, the error of H_r and E_r is relatively large. In the near-field, the error of H_ϕ is relatively large, and in the far-field, the error in the direction of θ and ϕ in both electric and magnetic fields show good agreement.

IV. COMPARISON WITH THE PEDAM

The PEDAM is derived in the Cartesian system [20]. The magnetic fields can be expressed as

$$H_x^m = K_h k_0 M_x [g_2(r) + \frac{-((y_m - y_n)^2 + (z_m - z_n)^2)}{r^2} \times g_1(r)] + K_h knn_0 Mn_y \frac{(x_m - x_n)(y_m - y_n)}{r^2} gnnn_1(r) + K_h knnn_0 Mnn_z \frac{(x_m - x_n)(z_m - z_n)}{r^2} gn_1(r), \quad (20)$$

$$H_y^m = K_h knn_0 Mnn_x \frac{(x_m - x_n)(y_m - y_n)}{r^2} g_1(r) + K_h knn_0 Mnn_y \times [g_2(r) + \frac{-((x_m - x_n)^2 + (z_m - z_n)^2)}{r^2} gn_1(r)] + K_h knn_0 Mnn_z \frac{(y_m - y_n)(z_m - z_n)}{r^2} gnn_1(r), \quad (21)$$

$$H_z^m = K_h knnn_0 Mnn_x \frac{(x_m - x_n)(z_m - z_n)}{r^2} gnn_1(r) + K_h knn_0 Mn_y \times \frac{(y_m - y_n)(z_m - z_n)}{r^2} gn_1(r) + K_h knn_0 Mnnn_z [g_2(r) + \frac{-((x_m - x_n)^2 + (z_m - z_n)^2)}{r^2} gnn_1(r)]. \quad (22)$$

The interval on the plane is $[-0.040m, 0.040m]$, and the interval is 0.005m on xoy plane, so there are $17 \times 17 = 289$ observation points. It is also assumed that the number of observation points is the same as the number of equivalent points. The measured surface radius $r_m = 0.062m$ and the optimal equivalent surface is $r_n = 0.055$. The near-field magnetic distribution at 0.072m and the far-field magnetic distribution at 1m were also compared. The results are shown in Fig. 9∼Fig. 12.

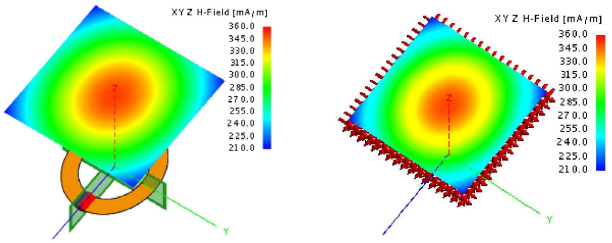

(a) Original magnetic field. (b) Equivalent magnetic field.

FIGURE 9. Comparison of magnetic field distribution at 0.062 m.

Fig. 9 shows the magnetic fields distribution of the MIMO ring antenna and the equivalent source on the near-field observation plane 0.062m. The magnetic fields distribution is roughly the same.

Fig. 10 shows the magnetic fields distribution of the MIMO ring antenna and the equivalent source on the observed plane

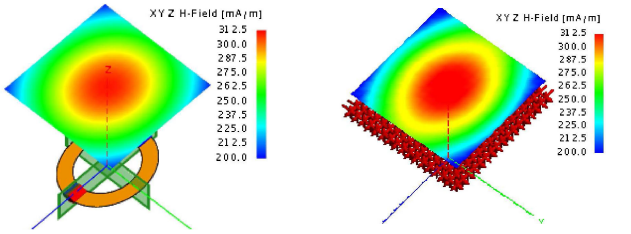

(a) Original magnetic field. (b) Equivalent magnetic field.

FIGURE 10. Comparison of magnetic field distribution at 0.072 m.

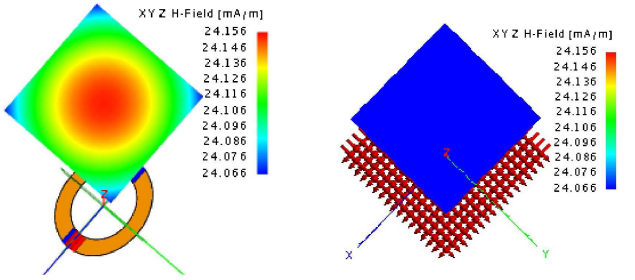

(a) Original magnetic field. (b) Equivalent magnetic field.

FIGURE 11. Comparison of magnetic field distribution at 1 m.

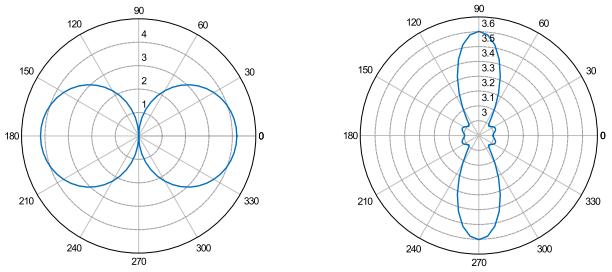

(a) Original model. (b) Equivalent model.

FIGURE 12. Comparison of far-field pattern at $\theta = 90°$, total E magnitude (V).

at 0.072m. The amplitude of the equivalent field in the middle part of the model is large.

Fig. 11 shows the magnetic fields distribution of the MIMO ring antenna and equivalent source on the observed plane at 1 m. The maximum magnetic fields value of the equivalent model is less than the original model on the whole plane.

The far-field direction patterns of the original model and the equivalent model are shown in Fig. 12 with $\theta = 90°$, which is quite different. According to the error shown in Table 3, it can also be seen that the error in the x direction of the far-field electric field is large. It's obvious that the direction distribution in Fig. 12 (a) and Fig. 12 (b) are totally different. For the far-field distribution of $\theta = 90°$, it is parallel to the xoy plane and is not in the main radiation direction of the PEDAM. At the same time, this model missing the fields information on xoz and yoz plane, so it is difficult to achieve effective prediction using the PEDAM.

It is worth noting that the SEDAM takes into account the diameter of the MIMO ring antenna, so the measured surface is 0.062m. However, when the measurement and equivalent surface of PEDAM is in reactive near-field region, the equivalent result is better than that in radiation near-field region.

When the measured surface is $r_m = 0.01m$ and the equivalent surface is $r_n = 0.001m$ using the PEDAM, the results are shown in Table 4. The equivalent errors are both less than 3%. This means that the PEDAM is applicable to the observation surface inside the reactive near-field region.

It can be seen that under the close equivalent surfaces of 0.05m and 0.055m, the error of PEDAM is larger than that of SEDAM. However, when the equivalent surface of the PEDAM is 0.001m, the equivalent result is better, which implies that the PEDAM is suitable for modeling in reactive near-field region. However, the distance 0.001m for the SEDAM is impossible, because the radius of the MIMO ring antenna is greater than 0.001m. Thus, the SEDAM is suitable for radiation near-field region modeling.

In order to compare the accuracy of the PEDAM and the proposed SEDAM, the following work is necessary. The first part is setting the SEDAM with the same observation plane and the same observation points with the PEDAM. The value interval on the observation plane is $[-0.040m, 0.040m]$, and the interval is 0.005m on xoy plane, so there are a total of $17 \times 17 = 289$ observation points, which is the same as the simulation setup in Section III. The other work is setting the PEDAM with the same observation sphere and the same observation points with the SEDAM, the same as the simulation setup in Section II. The range of θ is $1° \sim 179°$, ϕ is $0° \sim 330°$, and $7 \times 12 = 84$ observation points are selected at an interval of 30° both in θ and ϕ. Considering the size of the equivalent model itself, the observation surface here is the distance of 1 m from the MIMO ring antenna. The equivalent accuracy results are shown in Fig. 13.

As can be seen from Fig. 13 (a), the magnetic fields equivalent error of the proposed SEDAM at 1 m is larger, and the error of the electric fields is smaller than that obtained from the PEDAM. The 1 m distance is more concerned with the distribution of electric fields in practice. Therefore, in general, when the observation surface is plane, the SEDAM is preferable. It also can be seen from Fig. 13 (b) that the accuracy of the SEDAM is better than that of the PEDAM under the spherical observation.

The differences between these two methods including the following aspects. First of all, the accuracy of the equivalent modeling method is related to the distance of the near-field measurement. It can be seen from the results in Table 3 and Table 4 that the optimal modeling region of the PEDAM is the reactive near-field region, while the SEDAM is the radiation near-field region. The measured distance 0.062m is in the radiation near-field region of the MIMO ring antenna. Therefore, the accuracy of the SEDAM is better than that of the PEDAM. On the other hand, the PEDAM is mainly based on the near-field scanning results of the xoy plane, missing the field information of other positions in the space, which results in a large error in the far-field, especially as can be seen from Fig. 12 of the far-field direction patterns. Thirdly, the sparsity

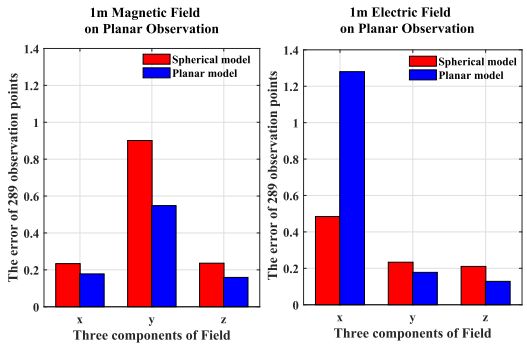

(a) The equivalent accuracy comparison of the two models while the observation is plane.

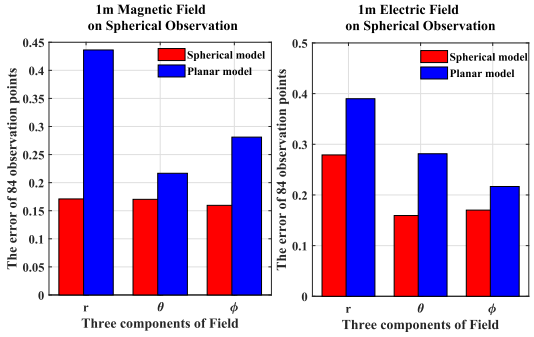

(b) The equivalent accuracy comparison of the two models while the observation is sphere.

FIGURE 13. The equivalent accuracy comparison of these two methods under different observation.

of the dipole array also directly affects the equivalent results. For example, there are 84 equivalent points in the SEDAM and 289 equivalent points in the PEDAM in Fig. 13 (a). Meanwhile, the observation points are 289. Therefore, the magnetic fields equivalent accuracy of PEDAM is better. In Fig. 13 (b), the SEDAM has 84 equivalent points, which equals to the number of spherical observation points, and the PEDAM has 289 equivalent points, which is more than the number of observation points. Therefore, the magnetic and electric fields equivalent accuracy of the SEDAM is better.

V. THE VERIFICATION OF MEASUREMENT

In this section, a workstation is used as the EUT. The measurement and observation distances are 0.48m and 0.55m respectively, and the measured frequency is $f = 504MHz$. In order to verify the accuracy of the proposed method in this paper, a spherical measurement device was developed. The device is made of PolymethylMethacrylate and the dielectric constant is 3.7. The measurement configurations are shown in Fig. 14 (a)∼(b).

On the measured hemispherical surface, the range of θ is $10° \sim 90°$, and the interval is 20°. The range of ϕ is $0° \sim 300°$, and the interval is 60°. Therefore, there are $5 \times 6 = 30$ discrete sampling points. Then the SEDAM could be used. In order to present the relatively continuous

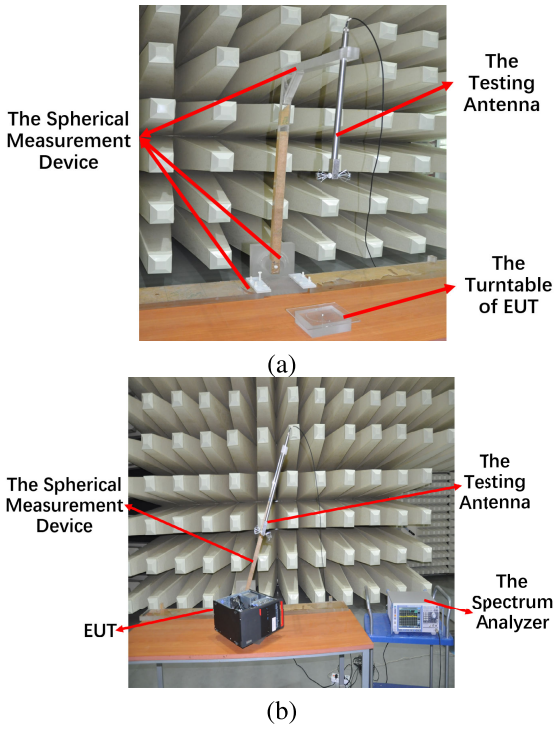

FIGURE 14. The spherical measurement device and the measurement site.

and smooth figures of electric and magnetic fields, which are shown in Fig. 15, we take the sampling interval of 5° both of θ and ϕ in Feko, that is, the sampling points of equivalent model on the observation surface are $19 \times 73 = 1387$. However, the error calculation is still the average of 30 measured sampling points where including 90 dipoles. The testing antenna is SBA 9113B small double hammer antenna, $80MHz \sim 3GHz$ SCHWARZBECK MESS, the Antenna Factor (AF) at $504MHz$ is $28dB/m$, which according to the product manual of schwarzbeck, German [25]. Before this, the measured data shall be preprocessed, and the formula as follows:

$$P(dBmW) = E(dB\mu V/m) - AF(dB/m) - 107 \quad (23)$$

The data of magnetic and electric fields predicted with the proposed method at an equivalent surface of 0.55m are shown in Fig. 15. The results for the measured equipment is in Table 5, which shows that the error between E_θ and H_ϕ, E_ϕ and H_θ are symmetric basically. Although affected by the testing accuracy and the fabrication error of the measurement device, the equivalent results have a large deviation, but still within the acceptable range. At the same time, we also find that the error near the poles on the hemispherical surface is relatively large.

In addition, in order to compare SEDAM with the PEDAM in this part. The distance of measured plane is also 0.48m. The sampling points value interval on the measured and observation plane are $x = [-0.20m, 0.20m]$, $y = [0m, 0.50m]$, and the interval is 0.1m on xoy plane, so there are also a total of $5 \times 6 = 30$ observation points. Calculated by

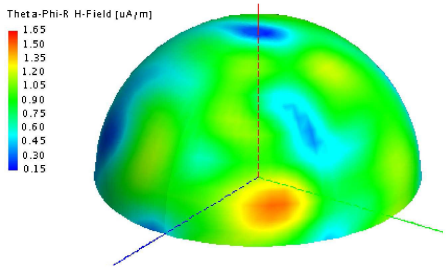

(a) The magnetic field distribution at 0.55m.

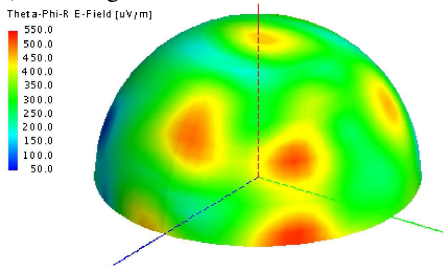

(b) The electric field distribution at 0.55m.

FIGURE 15. The equivalent magnetic and electric field distribution at 0.55 m.

TABLE 5. The error of 30 equivalent points.

Distance	0.48m magnetic	0.55m magnetic	0.55m electric
$Error(\theta)$	0.0257	0.3541	0.4143
$Error(\phi)$	0.0270	0.4630	0.3667

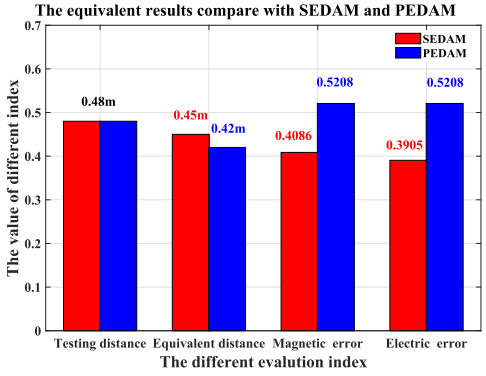

FIGURE 16. The comparison between the results obtained from the SEDAM and the PEDAM.

PEDAM, the distance of optimal equivalent plane is 0.42m. The equivalent results compare with SEDAM and PEDAM are shown in Fig. 16.

It can be seen from the equivalent results that the equivalent accuracy of the SEDAM is higher under the same measurement conditions, that is, the measured distance 0.48m is located in the radiation near-field region of EUT.

VI. CONCLUSION

In order to solve electromagnetic interference source location problems in electronic systems, this paper focuses on the near-field measurement of increasingly complex electronic equipments, and realizes the equivalent modeling with spherical dipole array. Only with accurate equivalence to complex electronic equipment can the feature recognition and interference location be realized.

The analytical relationship is derived between $H_r^m, H_\theta^m, H_\phi^m$ and the magnetic dipole moments M_r, M_θ, M_ϕ in the spherical coordinate system, then the MIMO Ring antenna is modeled using SEDAM. By comparing the results of the near-field magnetic fields, far-field magnetic/electric fields and far-field direction patterns with FEKO, it can be seen that the equivalent errors of the model are within 0.21, except for the r component in far-field, which shows good performance. The SEDAM is compared with the PEDAM, it is found that the PEDAM shows better accuracy in the reactive near-field region, but is not as high as that of the SEDAM at the same measured surface. Finally, the feasibility of the SEDAM is verified by the actual measurement of a workstation, in which, the results are also compared with the PEDAM.

The SEDAM is more suitable for large complex electromagnetic equipments, which can predict a spherical fields distribution in the near-field and far-field. The requirement for the scale of scanning points is small, and the SEDAM can realize the full space radiation field prediction for EUT. In addition, our proposed method is applicable for arbitrary electronic systems including circuit components with planar structure and packaging equipment with non-planar structures.

The limitation of the method in this paper is that the selection of sampling points should try to avoid the case that causes a large number of 0 in the relational matrix T, which will lead to a large deviation of the equivalent model due to the large condition number of T.

Further investigations to improve the accuracy near the poles and equator to find the optimal layout of sampling points and the prediction accuracy of equivalent model are in progress.

APPENDIX A
SPHERICAL EQUIVALENT DIPOLE ARRAY MODEL

Appendix A shows the theoretical derivation of the spherical equivalent dipole array, especially all the elements in the equivalent relation matrix.

$$\varepsilon_0 = \frac{1}{36\pi 10^9}, \tag{24}$$

$$\mu_0 = 4\pi 10^{-7}, \tag{25}$$

$$k_0 = \frac{2\pi}{\lambda}, \tag{26}$$

$$\omega = \frac{k_0}{\sqrt{\mu_0 \epsilon_0}}, \tag{27}$$

$$f(r) = \frac{e^{-jk_0 rn}}{r}, \tag{28}$$

$$K_h = \frac{k_0}{4\pi}, \tag{29}$$

$$g_1(r) = (\frac{3}{(k_0 rn)^2} + \frac{3j}{k_0 r} - 1)f(r), \tag{30}$$

$$g_2(r) = (\frac{2}{(k_0rnn)^2} + \frac{2j}{k_0rn})f(r), \tag{31}$$

$$g_3(r) = (\frac{1}{k_0rnn} + j)f(r). \tag{32}$$

$$\begin{aligned}T_{H_rMnn_r} =& (\sin\theta_m\cos\phi_m\sin\theta_n\cos\phi_n + \sin\theta_m\sin\phi_m\\ &\sin\theta_n\sin\phi_n + \cos\theta_m\cos\theta_n)g_2(r)\\ &+[\frac{-((y_m-y_n)^2+(z_m-z_n)^2)}{r^2}\sin\theta_m\cos\phi_m\\ &\sin\theta_n\cos\phi_n - \frac{(x_m-x_n)^2+(z_m-z_n)^2}{r^2}\\ &\sin\theta_m\sin\phi_m\sin\theta_n\sin\phi_n -\\ &\frac{(x_m-x_n)^2+(y_m-y_n)^2}{r^2}\cos\theta_m\cos\theta_n\\ &+\frac{(x_m-x_n)(y_m-y_n)}{r^2}(\sin\theta_m\cos\phi_m\sin\theta_n\\ &\sin\phi_n + \sin\theta_m\sin\phi_m\sin\theta_n\cos\phi_n)\\ &+\frac{(x_m-x_n)(z_m-z_n)}{r^2}(\sin\theta_m\cos\phi_m\cos\theta_n\\ &+\cos\theta_m\sin\theta_n\cos\phi_n) + \frac{(y_m-y_n)(z_m-z_n)}{r^2}\\ &(\sin\theta_m\sin\phi_m\cos\theta_n + \cos\theta_m\sin\theta_n\\ &\sin\phi_n)]g_1(r)\end{aligned} \tag{33}$$

$$\begin{aligned}T_{H_rMnn_\theta} =& (\sin\theta_m\cos\phi_m\cos\theta_n\cos\phi_n + \sin\theta_m\sin\phi_m\\ &\cos\theta_n\sin\phi_n - \cos\theta_m\sin\theta_n)g_2(r)\\ &+[\frac{-((y_m-y_n)^2+(z_m-z_n)^2)}{r^2}\sin\theta_m\cos\phi_m\\ &\cos\theta_n\cos\phi_n - \frac{(x_m-x_n)^2+(z_m-z_n)^2}{r^2}\\ &\sin\theta_m\sin\phi_m\cos\theta_n\sin\phi_n\\ &+\frac{(x_m-x_n)^2+(y_m-y_n)^2}{r^2}\cos\theta_m\sin\theta_n\\ &+\frac{(x_m-x_n)(y_m-y_n)}{r^2}(\sin\theta_m\cos\phi_m\cos\theta_n\\ &\sin\phi_n + \sin\theta_m\sin\phi_m\cos\theta_n\cos\phi_n)\\ &+\frac{(x_m-x_n)(z_m-z_n)}{r^2}(-\sin\theta_m\cos\phi_m\sin\theta_n\\ &+\cos\theta_m\cos\theta_n\cos\phi_n) + \frac{(y_m-y_n)(z_m-z_n)}{r^2}\\ &(-\sin\theta_m\sin\phi_m\sin\theta_n + \cos\theta_m\cos\theta_n\\ &\sin\phi_n)]g_1(r)\end{aligned} \tag{34}$$

$$\begin{aligned}T_{H_rMnn_\phi} =& (-\sin\theta_m\cos\phi_m\sin\phi_n + \sin\theta_m\sin\phi_m\\ &\cos\phi_n)g_2(r) + [\frac{(y_m-y_n)^2+(z_m-z_n)^2}{r^2}\\ &\sin\theta_m\cos\phi_m\sin\phi_n - \frac{(x_m-x_n)^2+(z_m-z_n)^2}{r^2}\\ &\sin\theta_m\sin\phi_m\cos\phi_n + \frac{(x_m-x_n)(y_m-y_n)}{r^2}\\ &(\sin\theta_m\cos\phi_m\cos\phi_n - \sin\theta_m\sin\phi_m\sin\phi_n)\\ &-\frac{(x_m-x_n)(z_m-z_n)}{r^2}\cos\theta_m\sin\phi_n)\\ &+\frac{(y_m-y_n)(z_m-z_n)}{r^2}\cos\theta_m\\ &\cos\phi_n)]g_1(r)\end{aligned} \tag{35}$$

$$\begin{aligned}T_{H_\theta Mnn_r} =& (\cos\theta_m\cos\phi_m\sin\theta_n\cos\phi_n + \cos\theta_m\sin\phi_m\\ &\sin\theta_n\sin\phi_n - \sin\theta_m\cos\theta_n)g_2(r)\\ &+[\frac{-((y_m-y_n)^2+(z_m-z_n)^2)}{r^2}\cos\theta_m\cos\phi_m\\ &\sin\theta_n\cos\phi_n - \frac{(x_m-x_n)^2+(z_m-z_n)^2}{r^2}\\ &\cos\theta_m\sin\phi_m\sin\theta_n\sin\phi_n\\ &+\frac{(x_m-x_n)^2+(y_m-y_n)^2}{r^2}\sin\theta_m\cos\theta_n\\ &+\frac{(x_m-x_n)(y_m-y_n)}{r^2}(\cos\theta_m\cos\phi_m\sin\theta_n\\ &\sin\phi_n + \cos\theta_m\sin\phi_m\sin\theta_n\cos\phi_n)\\ &+\frac{(x_m-x_n)(z_m-z_n)}{r^2}(\cos\theta_m\cos\phi_m\\ &\cos\theta_n - \sin\theta_m\sin\theta_n\cos\phi_n)\\ &+\frac{(y_m-y_n)(z_m-z_n)}{r^2}(\cos\theta_m\sin\phi_m\\ &\cos\theta_n - \sin\theta_m\sin\theta_n\sin\phi_n)]g_1(r)\end{aligned} \tag{36}$$

$$\begin{aligned}T_{H_\theta Mn_\theta} =& (\cos\theta_m\cos\phi_m\cos\theta_n\cos\phi_n + \cos\theta_m\\ &\sin\phi_m\cos\theta_n\sin\phi_n + \sin\theta_m\sin\theta_n)g_2(r)\\ &+[\frac{-((y_m-y_n)^2+(z_m-z_n)^2)}{r^2}\cos\theta_m\cos\phi_m\\ &\cos\theta_n\cos\phi_n - \frac{(x_m-x_n)^2+(z_m-z_n)^2}{r^2}\\ &\cos\theta_m\sin\phi_m\cos\theta_n\sin\phi_n\\ &-\frac{(x_m-x_n)^2+(y_m-y_n)^2}{r^2}\sin\theta_m\sin\theta_n\\ &+\frac{(x_m-x_n)(y_m-y_n)}{r^2}(\cos\theta_m\cos\phi_m\cos\theta_n\\ &\sin\phi_n + \cos\theta_m\sin\phi_m\cos\theta_n\cos\phi_n)\\ &-\frac{(x_m-x_n)(z_m-z_n)}{r^2}(\cos\theta_m\cos\phi_m\\ &\sin\theta_n + \sin\theta_m\cos\theta_n\cos\phi_n) -\\ &-\frac{(y_m-y_n)(z_m-z_n)}{r^2}(\cos\theta_m\sin\phi_m\\ &\sin\theta_n + \sin\theta_m\cos\theta_n\sin\phi_n)]g_1(r)\end{aligned} \tag{37}$$

$$\begin{aligned}T_{H_\theta Mn_\phi} =& (-\cos\theta_m\cos\phi_m\sin\theta_n + \cos\theta_m\sin\phi_m\\ &\cos\phi_n)g_2(r) + [\frac{(y_m-y_n)^2+(z_m-z_n)^2}{r^2}\\ &\cos\theta_m\cos\phi_m\sin\phi_n\\ &-\frac{(x_m-x_n)^2+(z_m-z_n)^2}{r^2}\cos\theta_m\sin\phi_m\\ &\cos\phi_n + \frac{(x_m-x_n)(y_m-y_n)}{r^2}(\cos\theta_m\\ &\cos\phi_m\cos\phi_n - \cos\theta_m\sin\phi_m\sin\phi_n)\\ &+\frac{(x_m-x_n)(z_m-z_n)}{r^2}\sin\theta_m\sin\phi_n)\\ &\frac{(y_m-y_n)(z_m-z_n)}{r^2}\sin\theta_m\\ &\cos\phi_n)]g_1(r)\end{aligned} \tag{38}$$

$$T_{H_\phi Mnnnn_r} = (\cos\phi_m \sin\theta_n \sin\phi_n - \sin\phi_m \sin\theta_n \cos\phi_n)g_2(r) + [\frac{(y_m - y_n)^2 + (z_m - z_n)^2}{r^2} \sin\phi_m \sin\theta_n \cos\phi_n - \frac{(x_m - x_n)^2 + (z_m - z_n)^2}{r^2} \cos\phi_m \sin\theta_n \cos\phi_n - \frac{(x_m - x_n)(y_m - y_n)}{r^2}(\cos\phi_m \sin\theta_n \sin\phi_n - \sin\phi_m \sin\theta_n \sin\phi_n) - \frac{(x_m - x_n)(z_m - z_n)}{r^2} \sin\phi_m \cos\theta_n + \frac{(y_m - y_n)(z_m - z_n)}{r^2} \cos\phi_m \cos\theta_n]g_1(r) \quad (39)$$

$$T_{H_\phi Mnnnn_\theta} = (\cos\phi_m \cos\theta_n \sin\phi_n - \sin\phi_m \cos\theta_n \cos\phi_n)g_2(r) + [\frac{(y_m - y_n)^2 + (z_m - z_n)^2}{r^2} \sin\phi_m \cos\theta_n \cos\phi_n - \frac{(x_m - x_n)^2 + (z_m - z_n)^2}{r^2} \cos\phi_m \cos\theta_n \sin\phi_n + \frac{(x_m - x_n)(y_m - y_n)}{r^2}(\cos\phi_m \cos\theta_n \cos\phi_n - \sin\phi_m \cos\theta_n \sin\phi_n) + \frac{(x_m - x_n)(z_m - z_n)}{r^2} \sin\phi_m \sin\theta_n - \frac{(y_m - y_n)(z_m - z_n)}{r^2} \cos\phi_m \sin\theta_n]g_1(r) \quad (40)$$

$$T_{H_\phi Mn_\phi} = (\cos\phi_m \cos\phi_n + \sin\phi_m \sin\phi_n)g_2(r) + [\frac{-((y_m - y_n)^2 + (z_m - z_n)^2)}{r^2} \sin\phi_m \sin\phi_n - \frac{(x_m - x_n)^2 + (z_m - z_n)^2}{r^2} \cos\phi_m \cos\phi_n - \frac{(x_m - x_n)(y_m - y_n)}{r^2}(\cos\phi_m \sin\phi_n + \sin\phi_m \cos\phi_n)]g_1(r) \quad (41)$$

ACKNOWLEDGMENT

The authors would like to appreciate the support and insightfully discussion with Hui Xu, Fan Zhang and Lilin Li at the School of Electronic and Information Engineering, Beihang University, Beijing, China.

REFERENCES

[1] D. Su, S. Xie, X. Shang, Z. Kaixiang, H. Xu, and A. X. Chen, "Basic emission waveform theory: A novel interpretation and source identification method for electromagnetic emission of complex systems," *IEEE Trans. Electromagn. Compat.*, vol. 60, no. 5, pp. 1330–1339, Oct. 2018.

[2] J. Wu, S. Cui, and D. Su, "Spectrum data feature analysis based on support vector machine method," in *Proc. Asia–Pacific Electromagn. Week Conf. Electromagn. Compat.*, 2017, pp. 1–3.

[3] G. Guo and L. Guo, "SBR method for near-field scattering of an electrically large complex target illuminated by dipole sources," *IEEE Access*, vol. 6, pp. 78710–78718, 2018.

[4] O. Neitz and T. F. Eibert, "A plane-wave synthesis approach for 3D monostatic RCS prediction from near-field measurements," in *Proc. 15th Eur. Radar Conf. (EuRAD)*, 2018, pp. 99–102.

[5] A. E. Sayers, W. M. Dorsey, K. W. O'Haver, and J. A. Valenzi, "Planar near-field measurement of digital phased arrays using near-field scan plane reconstruction," *IEEE Trans. Antennas Propag.*, vol. 60, no. 6, pp. 2711–2718, Jun. 2012.

[6] L. Zhang, L. Zhang, B. Wang, S. Liu, and C. Papavassiliou, "Hybrid prediction method for the electromagnetic interference characteristics of printed circuit boards based on the equivalent dipole model and the finite-difference time domain method," *IEEE Access*, vol. 6, pp. 6520–6529, 2017.

[7] R. Cornelius and D. Heberling, "Spherical near-field scanning with pointwise probe correction," *IEEE Trans. Antennas Propag.*, vol. 65, no. 2, pp. 995–997, Feb. 2017.

[8] F. Saccardi, A. Giacomini, L. M. Tancioni, and L. J. Foged, "Full probe corrected spherical near field measurement technique using standard wideband antennas as probes," in *Proc. 12th Eur. Conf. Antennas Propag. (EuCAP)*, 2018, pp. 9–13.

[9] J. R. Camacho-Perez and P. Moreno, "Initial considerations towards hemispherical near-field antenna measurement," *IEEE Antennas Wireless Propagat. Lett.*, vol. 13, pp. 1441–1444, 2014.

[10] F. S. de Adana, M. F. Cátedra, J. M. Gómez, R. Mittra, J. B. Renuncio, F. Gutiérrez, and M. A. Prieto, "An effective technique for system-level prediction of the radiated emissions of unknown sources inside Low-*Q* cavities using unit-level measurements," *IEEE Trans. Electromagn. Compat.*, vol. 51, no. 2, pp. 181–191, May 2009.

[11] F. S. de Adana, M. F. Catedra, J. M. Gomez, and R. Mittra, "Effective technique for system level prediction of the radiated emissions of electronic devices and cables inside satellites from unit level measurements," in *Proc. IEEE Int. Symp. Electromagn. Compat.*, Jul. 2007, pp. 1–5.

[12] X. Tong, "Simplified equivalent modelling of electromagnetic emissions from printed circuit boards," Ph.D. dissertation, Dept. Elect. Electron. Eng., Univ. Nottingham, Nottingham, U.K., 2010.

[13] X. Tong, D. W. P. Thomas, A. Nothofer, P. Sewell, and C. Christopoulo, "Modeling electromagnetic emissions from printed circuit boards in closed environments using equivalent dipoles," *IEEE Trans. Electromagn. Compat.*, vol. 52, no. 2, pp. 462–470, May 2010.

[14] G.-H. Sun, S.-W. Wong, and H. Wong, "A broadband antenna array using full-wave dipole," *IEEE Access*, vol. 5, pp. 13054–13061, 2017.

[15] P. F. Lopez, C. Arcambal, D. Baudry, S. Verdeyme, and B. Mazari, "Simple electromagnetic modeling procedure: From near-field measurements to commercial electromagnetic simulation tool," *IEEE Trans. Instrum. Meas.*, vol. 59, no. 12, pp. 3111–3121, Dec. 2010.

[16] H. Weng, D. G. Beetner, and R. E. DuBroff, "Prediction of radiated emissions using near-field measurements," *IEEE Trans. Electromagn. Compat.*, vol. 53, no. 4, pp. 891–899, Nov. 2011.

[17] Z. Yu, J. A. Mix, S. Sajuyigbe, K. P. Slattery, and J. Fan, "An improved dipole-moment model based on near-field scanning for characterizing near-field coupling and far-field radiation from an IC," *IEEE Trans. Electromagn. Compat.*, vol. 55, no. 1, pp. 97–108, Feb. 2013.

[18] K.-Y. See, N. Fang, L.-B. Wang, W. Soh, T. Svimonishvili, M. Oswal, W.-Y. Chang, and W.-J. Koh, "An empirical approach to develop near-field limit for radiated-emission compliance check," *IEEE Trans. Electromagn. Compat.*, vol. 56, no. 3, pp. 691–698, Jun. 2014.

[19] S. M. Mikki, S. Clauzier, and Y. M. M. Antar, "Empirical geometrical bounds on MIMO antenna arrays for optimum diversity gain performance: An electromagnetic design approach," *IEEE Access*, vol. 6, pp. 39876–39894, 2018.

[20] J. Pan, H. Wang, X. Gao, C. Hwang, E. Song, H.-B. Park, and J. Fan, "Radio-frequency interference estimation using equivalent dipole-moment models and decomposition method based on reciprocity," *IEEE Trans. Electromagn. Compat.*, vol. 58, no. 1, pp. 75–84, Feb. 2016.

[21] Q. Huang and J. Fan, "Machine learning based source reconstruction for RF desense," *IEEE Trans. Electromagn. Compat.*, vol. 60, no. 6, pp. 1640–1647, Dec. 2018.

[22] F.-P. Xiang, E.-P. Li, X.-C. Wei, and J.-M. Jin, "A particle swarm optimization-based approach for predicting maximum radiated emission from PCBs with dominant radiators," *IEEE Trans. Electromagn. Compat.*, vol. 57, no. 5, pp. 891–899, Oct. 2015.

[23] W. Kong and E.-P. Li, "Prediction of PCB radiated emission in shielding cavity using equivalent dipole modeling," in *Proc. IEEE Int. Symp. Electromagn. Compat.*, Aug. 2015, pp. 1484–1488.

[24] P. Wilson, "On correlating TEM cell and OATS emission measurements," *IEEE Trans. Electromagn. Compat.*, vol. 37, no. 1, pp. 1–16, Feb. 1995.

[25] *Microwave Biconical Antenna SBA 9113 B*. [Online]. Available: http://www.schwarzbeck.com/index.php/en/antennas/biconical-antennas SBA9113B

JING NIE received the B.S. and M.S. degrees in applied mathematics from the North University of China, China, in 2010 and 2013, respectively. She is currently pursuing the Ph.D. degree in electromagnetic compatibility and electromagnetic environment with Beihang University, Beijing, China.

Her current research interests include electromagnetic compatibility evaluation in system level and electromagnetic radiation modeling of equipment.

SHUNCHUAN YANG received the B.S. degree from Sichuan University, China, in 2009, the M.S. degree from Zhejiang University, China, in 2012, and the Ph.D. degree from Dalhousie University, Canada, in 2015.

He joined Beihang University, as an Associate Professor, in 2017. His research interests include development of advanced numerical methods for computational electromagnetics (CEM) both in time and frequency domains and their applications in integrated circuits modeling, multiphysics, and complex media modeling. He was a recipient of the Killam Awards of Dalhousie University, in 2014, and the Chinese Government Award for Outstanding Self-financed Students Abroad, in 2013.

DONGLIN SU (M'96) received the B.S., M.S., and Ph.D. degrees in electrical engineering from Beihang University (BUAA), Beijing, China, in 1983, 1986, and 1999, respectively.

In 1986, she joined the Faculty of School of Electronics and Information Engineering, BUAA, where she was first an Assistant, then a Lecturer, later on an Associate Professor, and is currently a Full Professor. From 1996 to 1998, she was a Visiting Scholar with the Department of Electrical Engineering, University of California at Los Angeles (UCLA), Los Angeles, CA, USA, under the BUAA–UCLA Joint Ph.D. Program. She has authored more than 100 papers and coauthored several books. Her research interests include the numerical methods for microwave and millimeter-wave integrated circuits and systematic electromagnetic compatibility design of various aircrafts.

Dr. Su is a Senior Member of the Chinese Institute of Electronics. She is the Chair of Beijing Chapter of the IEEE Antennas and Propagation Society and the Deputy Chair of the Antennas Society, Chinese Institute of Electronics. She was a recipient of the two National Awards for Science and Technology Progress, in 2007 and 2012, respectively.